

Pressure-driven flows in helical pipes: bounds on flow rate and friction factor

Anuj Kumar¹†

¹Department of Applied Mathematics, Baskin School of Engineering, University of California, Santa Cruz, CA 95064, USA

(Received xx; revised xx; accepted xx)

In this paper, we use the well-known background method to obtain a rigorous lower bound on the volume flow rate through a helical pipe driven by a pressure differential in the limit of large Reynolds number. As a consequence, we also obtain an equivalent upper bound on the friction factor. These bounds are also valid for toroidal and straight pipes as limiting cases. By considering a two-dimensional background flow with varying boundary layer thickness along the circumference of the pipe, we obtain these bounds as a function of the curvature and torsion of the pipe and therefore capture the geometrical aspects of the problem. In this paper, we also present a sufficient criterion to find out which pressure-driven flow and surface-velocity-driven flow problems can be tackled using the background method.

Key words:

1. Introduction

Curved pipes have a wide range of applications in the industry because of their enhanced mixing properties, high heat transfer coefficient, and compact structure. Examples of application include, but are not limited to, heat exchangers, air-conditioning systems, chemical reactors, and steam generators (see the review by Vashisth *et al.* 2008; Naphon & Wongwises 2006). One of the crucial questions in the study of turbulent flows in curved pipes is the accurate determination of the dependence of the flow rate and friction factor on the applied pressure difference between the two ends of the pipe, and its dependence on geometrical parameters such as the pipe's curvature and torsion. The extensive usage of curved pipes in the industry has motivated many studies to characterize this dependence (see Itō 1959; Liu & Masliyah 1993; Yamamoto *et al.* 1994, 1995; Cioncolini & Santini 2006). However, only a few of these studies consider the high Reynolds number limit, which is the objective of this paper.

The flow structure inside a curved pipe can vary substantially with Reynolds number and pipe geometry, which leads to a number of different regimes, each with its own distinct functional dependence of the flow rate and friction factor on these parameters. As such, quantifying this dependence becomes difficult even for the laminar flow, unlike the case of a straight pipe. Indeed, at low Reynolds number, an imbalance between centrifugal force and cross-stream pressure leads to the onset of secondary counter-rotating vortices known as Dean's vortices, which were first experimentally observed by Eustice (1910, 1911). Dean (1927, 1928) confirmed this observation analytically in the low curvature limit

† Email address for correspondence: akumar43@ucsc.edu

by computing the flow velocity as a perturbation of the well-known laminar Poiseuille flow solution. Dean (1928) showed that the effect of curvature is to decrease the flow rate and that this effect is of second-order, i.e. quadratic in curvature. Several other studies were performed in the limit of small curvature to obtain a steady-state flow solution in a toroidal pipe, see for example, McConalogue & Srivastava (1968); Van Dyke (1978); Dennis (1980). For a comprehensive review of the topic, the reader is referred to Berger *et al.* (1983). Germano (1982) further extended Dean's result to a helical pipe with small torsion and Tuttle (1990) showed that small torsion leads to a second-order decrease in the flow rate. However, no analytical result exists for the steady flow in a pipe with a finite radius of curvature or torsion. Therefore, even in the laminar regime, one has to rely on empirical formulae to quantify the flow rate.

The transition to turbulence in curved pipes also differs substantially from the case of a straight pipe. Taylor (1929) and White (1929) found that flow in a curved pipe is more stable than in a straight pipe. Notably, they saw that the critical Reynolds number for the transition is twice as large as in the straight pipe case. Inspired by this observation, Sreenivasan & Strykowski (1983) conducted experiments in a straight tube followed by a helical tube with curvature $\kappa = 0.058$. They noticed an oscillating behavior near the inner wall of the helical tube at a moderate Reynolds number, which Webster & Humphrey (1993, 1997) attributed to the presence of traveling wave perturbations to the Dean's vortices. Recent years have witnessed a resurgence in carefully conducted studies to quantify the effect of curvature on the stability of flow in a torus. Kühnen *et al.* (2015) studied this problem using a novel experimental setup where a magnetically controlled steel sphere drives the flow in a torus. They conjectured that the transition switches from subcritical to supercritical for a critical torus curvature $\kappa \simeq 0.028$. Soon after that, Canton *et al.* (2016) performed an in-depth linear stability analysis, covering the entire curvature range, and obtained the critical Reynolds number as a function of the curvature. More recently, Canton *et al.* (2020) have shed light on the complexity of transition for flow in a torus, demonstrating in particular that for $\kappa \simeq 0.025$, two branches of solution can coexist at the same Reynolds number: one with subcritically-excited sustained turbulence, and the other consisting of a low-amplitude travelling wave originating from a supercritical Hopf bifurcation.

The incredible complexity of curved pipe flows makes it impossible to obtain the precise dependence of mean quantities such as flow rate or friction factor on model parameters. This is especially true at high Reynolds number, where both laboratory experiments and numerical computations are extremely challenging and must be repeated for different pipe geometries. As noted by Vester *et al.* (2016), the determination of the friction factor (or equivalently the flow rate) for turbulent flows in curved pipes has generally been neglected, with only a few exceptions (Itō 1959; Cioncolini & Santini 2006). However, as we shall demonstrate in this paper, it is possible to obtain bounds on these mean quantities as explicit functions of flow and geometric variables, in the high Reynolds number limit.

Obtaining bounds on mean quantities in fluid mechanics goes back to the classical technique of Howard (1963), which was further developed by Busse (1969, 1970). In the 1990s, Doering and Constantin (Doering & Constantin 1992, 1994; Constantin & Doering 1995; Doering & Constantin 1996), based on the ideas from Hopf (1957), developed a new technique known as the background method to bound mean quantities. This method requires a careful choice of a trial function (the background field) to satisfy a spectral constraint in order to obtain a bound on the desired quantity. Since the work of Doering and Constantin, this method has been applied to a wide variety of problems in fluid dynamics. Examples include upper bounds on

the rate of energy dissipation in surface-velocity-driven flows (Doering & Constantin 1992, 1994; Marchioro 1994; Wang 1997; Plasting & Kerswell 2003), pressure-driven flows (Constantin & Doering 1995), and surface-stress-driven flows (Tang *et al.* 2004; Hagstrom & Doering 2014); upper bounds on the heat transfer in different configurations of Rayleigh–Bénard convection (Doering & Constantin 1996, 2001; Otero *et al.* 2002; Plasting & Ierley 2005; Wittenberg 2010; Whitehead & Doering 2011; Whitehead & Wittenberg 2014; Goluskin 2015; Goluskin & Doering 2016; Fantuzzi 2018) and Bénard–Marangoni convection (Hagstrom & Doering 2010; Fantuzzi *et al.* 2018, 2020); upper bounds on buoyancy flux in stably stratified shear flows (Caulfield & Kerswell 2001; Caulfield 2005).

In this paper, we use this background method to obtain a lower bound on the flow rate and an equivalent upper bound on friction factor for flows in helical pipes. The novelty in this paper is the use of a two-dimensional background flow in contrast with most previous applications of the background method, where the geometry was simple enough to use a one-dimensional background flow to suffice the desired purpose. We start by setting up the problem in §2, where we describe the flow configuration and the coordinate system used to solve the problem. In §3, we formulate the background method in the context of pressure-driven flows in helical pipes. In §4, we choose the background flow and obtain bounds on the flow rate and friction factor. Finally, in §5, we compare our findings with available experimental data and make a few remarks about the applicability of the background method to other interesting problems in engineering.

2. Problem Setup

2.1. Flow configuration

We consider the flow of an incompressible fluid with density ρ and kinematic viscosity ν in a helical pipe. The radius of the pipe is denoted as R_p , the radius of the centerline helix R_h , and the pitch of the centerline helix is $2\pi l$ (see figure 1a). Here, the centerline helix refers to the locus of the center of the pipe. The flow is driven by a body force \mathbf{f}^* , which has dimensional amplitude F . The choice of forcing is described in §2.3. We non-dimensionalize the variables as follows

$$\mathbf{f} = \frac{\mathbf{f}^*}{F}, \quad \mathbf{u} = \left(\frac{\rho}{FR_p} \right)^{\frac{1}{2}} \mathbf{u}^*, \quad p = \frac{p^* - p_a}{FR_p}, \quad \mathbf{x} = \frac{\mathbf{x}^*}{R_p}, \quad t = \left(\frac{F}{\rho R_p} \right)^{\frac{1}{2}} t^*. \quad (2.1)$$

Here, p_a is the ambient pressure, whereas \mathbf{f} , \mathbf{u} , p , \mathbf{x} , and t denote the non-dimensional forcing, velocity, pressure, position, and time, respectively. Quantities with a star in superscript are dimensional. The equations governing the flow in non-dimensional form are as follows

$$\begin{aligned} \nabla \cdot \mathbf{u} &= 0, \\ \frac{\partial \mathbf{u}}{\partial t} + \mathbf{u} \cdot \nabla \mathbf{u} &= -\nabla p + \frac{1}{Re} \nabla^2 \mathbf{u} + \mathbf{f}, \end{aligned} \quad (2.2)$$

where

$$Re = \frac{R_p}{\nu} \left(\frac{FR_p}{\rho} \right)^{\frac{1}{2}}$$

is the Reynolds number. The boundary conditions at the surface of the pipe are no-slip and impermeable.

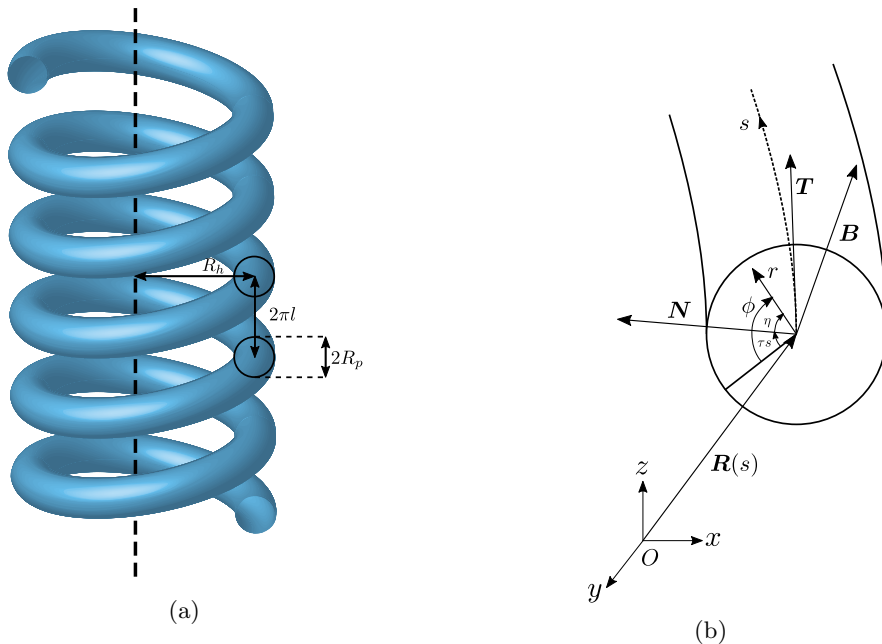


Figure 1: (a) Schematic diagram of a helical pipe with radius R_p , radius of the centerline helix R_h , and pitch of the centerline helix $2\pi l$. The dashed line is the axis of rotation of the helical pipe. (b) Illustration of the coordinate system (s, r, ϕ) used in this paper.

2.2. Coordinate system

In this subsection, we construct an orthogonal coordinate system that is well-suited for our problem. This coordinate system was first introduced by Germano (1982), who was interested in the effect of small torsion on Dean's solution. The coordinate system has been extensively used since then in both analytical and computational studies of flows in helical pipes (Kao 1987; Germano 1989; Tuttle 1990; Liu & Masliyah 1993; Yamamoto *et al.* 1994; Hüttl & Friedrich 2001; Gammack & Hydon 2001). For clarity and self-consistency, we repeat its construction below.

Let a and $2\pi b$ be the non-dimensional centerline helix radius and pitch, where $a = R_h/R_p$ and $b = l/R_p$. The equation of this helix parameterized with arc length s in a Cartesian coordinate system (x, y, z) is given by

$$(x(s), y(s), z(s)) = \left(a \cos\left(\frac{s}{\sqrt{a^2 + b^2}}\right), a \sin\left(\frac{s}{\sqrt{a^2 + b^2}}\right), \frac{bs}{\sqrt{a^2 + b^2}} \right). \quad (2.3)$$

Let $\mathbf{R}(s) = (x(s), y(s), z(s))$ be the position vector and let $\mathbf{T}(s)$, $\mathbf{N}(s)$, and $\mathbf{B}(s)$ be the tangent, normal, and binormal to the centerline helix, which are given by

$$\mathbf{T} = \frac{d\mathbf{R}}{ds}, \quad \mathbf{N} = \frac{1}{\kappa} \frac{d\mathbf{T}}{ds}, \quad \mathbf{B} = \mathbf{T} \times \mathbf{N}. \quad (2.4)$$

The relations among the tangent, normal, and binormal are given by the Frenet–Serret formulae, which are

$$\frac{d\mathbf{N}}{ds} = \tau\mathbf{B} - \kappa\mathbf{T}, \quad \frac{d\mathbf{B}}{ds} = -\tau\mathbf{N}, \quad (2.5)$$

where

$$\kappa = \frac{a}{a^2 + b^2}, \quad \text{and} \quad \tau = \frac{b}{a^2 + b^2} \quad (2.6)$$

are the non-dimensional curvature and torsion of the helix. The curvature is considered smaller than one ($\kappa < 1$) in this paper. We now construct a coordinate system (s, r, η) such that any Cartesian position vector \mathbf{x} can be expressed as

$$\mathbf{x} = \mathbf{R} + r \cos \eta \mathbf{N} + r \sin \eta \mathbf{B}. \quad (2.7)$$

With the use of (2.4) and (2.5),

$$d\mathbf{x} \cdot d\mathbf{x} = [(1 - r\kappa \cos \eta)^2 + \tau^2 r^2] ds^2 + dr^2 + r^2 d\eta^2 + 2\tau r^2 ds d\eta. \quad (2.8)$$

Therefore, the resulting coordinate system is non-orthogonal. However, using the transformation $\eta = \phi - \tau s$ in (2.8), we obtain

$$d\mathbf{x} \cdot d\mathbf{x} = (1 - r\kappa \cos(\phi - \tau s))^2 ds^2 + dr^2 + r^2 d\phi^2. \quad (2.9)$$

The coordinate system (s, r, ϕ) is orthogonal, and will be used to perform calculations in the rest of the paper. The scale factors for this coordinate system are defined as

$$h_s = (1 - r\kappa \cos(\phi - \tau s)), \quad h_r = 1, \quad h_\phi = r. \quad (2.10)$$

The impermeability and no-slip condition at the surface of the pipe in the (s, r, ϕ) coordinate system translate to

$$\mathbf{u} = (u_s, u_r, u_\phi) = \mathbf{0} \text{ at } r = 1. \quad (2.11)$$

In this paper, we assume that the flow is periodic in the streamwise direction s with period s_p . Hence, the domain of interest in the (s, r, ϕ) coordinate system is

$$\Omega = [0, s_p] \times [0, 1] \times [0, 2\pi]. \quad (2.12)$$

2.3. Choice of forcing

We choose to drive the flow with a dimensional forcing

$$\mathbf{f}^* = -\frac{1}{1 - r^* \kappa^* \cos(\phi^* - \tau^* s^*)} \times \frac{dP}{ds^*} \mathbf{e}_s \quad \text{for } 0 \leq r^* \leq R_p. \quad (2.13)$$

Here, $-dP/ds^*$ is a constant and can be thought of as the applied pressure gradient. Note how this streamwise directed forcing varies across the cross-section. The reason for this choice of forcing over a conventional forcing, which would be constant across the cross-section, is that the line integral along the streamwise direction for this forcing is independent of the position on the pipe cross-section and depends only on the difference of streamwise coordinates, i.e.

$$\int_{s^*=s_1^*}^{s^*=s_2^*} \mathbf{f}^* \cdot \mathbf{e}_s dl = \int_{s^*=s_1^*}^{s^*=s_2^*} -\frac{dP}{ds^*} ds^* = -\frac{dP}{ds^*} (s_2^* - s_1^*), \quad (2.14)$$

where $dl = h_s^* ds^*$ is the line element with $h_s^* = 1 - r^* \kappa^* \cos(\phi^* - \tau^* s^*)$. By contrast, for the conventional forcing, the value of this line integral would also depend on the position on the cross-section. Hence, we believe that our choice of forcing is good for modeling a flow driven by constant pressure boundary conditions. More detail on this choice of forcing in the context of flow in a torus can be found in Canton *et al.* (2016, 2017); Rinaldi *et al.* (2019). Note that in the limit of vanishing curvature ($\kappa \rightarrow 0$), our choice does reduce to constant forcing in the streamwise direction and therefore is consistent

with the usual modeling of pressure-driven flow in a straight pipe. Based on (2.13), we define the forcing scale as

$$F = -\frac{dP}{ds^*}.$$

This implies that the non-dimensional forcing is given by

$$\mathbf{f} = \frac{1}{1 - r\kappa \cos(\phi - \tau s)} \mathbf{e}_s \quad \text{for } 0 \leq r \leq 1. \quad (2.15)$$

2.4. Quantities of interest

We are interested in obtaining a lower bound on the average non-dimensional flow rate Q , which we simply call flow rate, and an equivalent upper bound on the friction factor λ in the limit of high Reynolds number. As we are concerned with the high Reynolds number limit, so we use an inertial scaling to define the non-dimensional flow rate Q as

$$Q = \frac{1}{R_p^2} \left(\frac{\rho}{FR_p} \right)^{\frac{1}{2}} Q^* = \left\langle \int_{\phi=0}^{2\pi} \int_{r=0}^1 u_s r dr d\phi \right\rangle, \quad (2.16)$$

where Q^* is the long-time average of the dimensional flow rate, u_s is the streamwise component of the non-dimensional velocity field \mathbf{u} and

$$\langle [\cdot] \rangle = \lim_{T \rightarrow \infty} \frac{1}{T} \int_{t=0}^T [\cdot] dt \quad (2.17)$$

denotes the long-time average of a quantity. The Darcy–Weisbach friction factor λ , which is four times the Fanning friction factor, is defined as

$$\lambda = -\frac{dP}{ds^*} \frac{4R_p}{\rho u_m^{*2}}, \quad (2.18)$$

where u_m^* is the dimensional streamwise mean velocity given by

$$u_m^* = \frac{Q^*}{\pi R_p^2}. \quad (2.19)$$

When expressed in non-dimensional variables, the friction factor is

$$\lambda = \frac{4\pi^2}{Q^2}. \quad (2.20)$$

From (2.20), we notice that a lower bound on the flow rate Q will provide an upper bound on the friction factor λ .

3. The background method formulation

In this section, we describe the general approach of the background method applied to our problem. The formulation that we develop here is for any general background flow field and is similar to the one given in Constantin & Doering (1995) for pressure-driven channel flow.

The background method, in essence, works as follows. We first derive time-averaged integral identities from the governing equations (2.2) (using the fact that the long-time averages of certain time derivatives vanish) in order to rewrite the quantity of interest Q given by (2.16) as an equivalent long-time averaged expression that is easier to bound using analysis techniques. To that end, we begin by establishing a time-averaged

total energy equation, by taking the dot product of equation (2.2) with \mathbf{u} and then by performing a volume integration on the resulting equation. The result is

$$\frac{1}{2} \frac{d\|\mathbf{u}\|_2^2}{dt} = -\frac{1}{Re} \|\nabla\mathbf{u}\|_2^2 + \int_{\Omega} \mathbf{f} \cdot \mathbf{u} \, d\mathbf{x}, \quad (3.1)$$

where $\|\cdot\|_2$ denotes the L^2 -norm, which is given by

$$\|\cdot\|_2 = \left(\int_{\Omega} |\cdot|^2 \, d\mathbf{x} \right)^{\frac{1}{2}}, \quad (3.2)$$

and where the volume integral in (s, r, ϕ) coordinates is written as

$$\int_{\Omega} [\cdot] \, d\mathbf{x} = \int_{s=0}^{s_p} \int_{\phi=0}^{2\pi} \int_{r=0}^1 [\cdot] h_s h_r h_{\phi} dr d\phi ds. \quad (3.3)$$

The quantity $\|\mathbf{u}\|_2^2(t)$ can be shown to be uniformly bounded in time within the framework of the background method (see Doering & Constantin 1992; Constantin & Doering 1995, for example). Therefore, the long-time average of the time derivative of $\|\mathbf{u}\|_2^2(t)$ vanishes. As a result, taking the long-time average of equation (3.1) leads to

$$\left\langle \int_{\Omega} \mathbf{f} \cdot \mathbf{u} \, d\mathbf{x} \right\rangle = \frac{1}{Re} \langle \|\nabla\mathbf{u}\|_2^2 \rangle. \quad (3.4)$$

The second step of the method is to perform the background decomposition. We start by writing the total velocity \mathbf{u} as the sum of two divergence-free velocity fields $\mathbf{u} = \mathbf{U} + \mathbf{v}$, where $\nabla \cdot \mathbf{U} = 0$ and $\nabla \cdot \mathbf{v} = 0$. We call \mathbf{U} the background flow, which is steady and satisfies the same boundary conditions as the full flow \mathbf{u} , while the perturbation \mathbf{v} satisfies the homogeneous version of the boundary conditions. The equation governing the evolution of \mathbf{v} is given by

$$\frac{\partial \mathbf{v}}{\partial t} + \mathbf{U} \cdot \nabla \mathbf{U} + \mathbf{U} \cdot \nabla \mathbf{v} + \mathbf{v} \cdot \nabla \mathbf{U} + \mathbf{v} \cdot \nabla \mathbf{v} = -\nabla p + \frac{1}{Re} \nabla^2 \mathbf{U} + \frac{1}{Re} \nabla^2 \mathbf{v} + \mathbf{f}. \quad (3.5)$$

Taking the dot product of the above equation with \mathbf{v} and performing a volume integration, followed by taking the long-time average, results in

$$\left\langle \int_{\Omega} \mathbf{f} \cdot \mathbf{v} \, d\mathbf{x} \right\rangle = \frac{1}{2Re} \langle \|\nabla\mathbf{u}\|_2^2 \rangle - \frac{1}{2Re} \|\nabla\mathbf{U}\|_2^2 + \langle \mathcal{H}(\mathbf{v}) \rangle, \quad (3.6)$$

where

$$\mathcal{H}(\mathbf{v}) = \underbrace{\int_{\Omega} (\mathbf{v} \cdot \nabla \mathbf{U}_{\text{sym}}) \cdot \mathbf{v} \, d\mathbf{x}}_I + \underbrace{\int_{\Omega} (\mathbf{U} \cdot \nabla \mathbf{U}) \cdot \mathbf{v} \, d\mathbf{x}}_{II} + \underbrace{\frac{1}{2Re} \|\nabla\mathbf{v}\|_2^2}_{III}, \quad (3.7)$$

and $\nabla\mathbf{U}_{\text{sym}}$ is the symmetric part of $\nabla\mathbf{U}$, i.e.

$$\nabla\mathbf{U}_{\text{sym}} = \frac{\nabla\mathbf{U} + \nabla\mathbf{U}^{\top}}{2}. \quad (3.8)$$

We have used the following identity in deriving the equation (3.6)

$$|\nabla\mathbf{u}|^2 = |\nabla\mathbf{U}|^2 + |\nabla\mathbf{v}|^2 + 2\nabla\mathbf{U} : \nabla\mathbf{v}, \quad (3.9)$$

where, in index notation,

$$\nabla\mathbf{U} : \nabla\mathbf{v} = \partial_i v_j \partial_i U_j. \quad (3.10)$$

Multiplying (3.6) by two and subtracting (3.4) yields

$$2 \left\langle \int_{\Omega} \mathbf{f} \cdot \mathbf{v} \, d\mathbf{x} \right\rangle - \left\langle \int_{\Omega} \mathbf{f} \cdot \mathbf{u} \, d\mathbf{x} \right\rangle = -\frac{1}{Re} \|\nabla \mathbf{U}\|_2^2 + 2 \langle \mathcal{H}(\mathbf{v}) \rangle. \quad (3.11)$$

The left-hand side of (3.11) can be simplified as follows

$$\begin{aligned} & 2 \left\langle \int_{\Omega} \mathbf{f} \cdot \mathbf{v} \, d\mathbf{x} \right\rangle - \left\langle \int_{\Omega} \mathbf{f} \cdot \mathbf{u} \, d\mathbf{x} \right\rangle = \left\langle \int_{\Omega} \mathbf{f} \cdot \mathbf{u} \, d\mathbf{x} \right\rangle - 2 \left\langle \int_{\Omega} \mathbf{f} \cdot \mathbf{U} \, d\mathbf{x} \right\rangle \\ & = \left\langle \int_{s=0}^{s_p} \left[\int_{\phi=0}^{2\pi} \int_{r=0}^1 u_s r \, dr \, d\phi \right] ds \right\rangle - 2 \int_{s=0}^{s_p} \left[\int_{\phi=0}^{2\pi} \int_{r=0}^1 U_s r \, dr \, d\phi \right] ds \\ & = s_p \left\langle \int_{\phi=0}^{2\pi} \int_{r=0}^1 u_s r \, dr \, d\phi \right\rangle - 2 s_p \int_{\phi=0}^{2\pi} \int_{r=0}^1 U_s r \, dr \, d\phi. \end{aligned} \quad (3.12)$$

Note that we used $\mathbf{v} = \mathbf{u} - \mathbf{U}$ in the first line, then substituted the expression for \mathbf{f} from (2.15) and used the time independence of \mathbf{U} to obtain the second line. The terms in the square brackets in the second line represent the flow of \mathbf{u} and \mathbf{U} through a cross-section of pipe and therefore are independent of the streamwise direction s because of the incompressibility of \mathbf{u} and \mathbf{U} . Hence, we can easily integrate these expressions with respect to s , which leads to the third line. Using (3.12) in (3.11) and dividing by s_p on both sides gives

$$Q = \left\langle \int_{\phi=0}^{2\pi} \int_{r=0}^1 u_s r \, dr \, d\phi \right\rangle = 2 \int_{\phi=0}^{2\pi} \int_{r=0}^1 U_s r \, dr \, d\phi - \frac{1}{s_p Re} \|\nabla \mathbf{U}\|_2^2 + \frac{2}{s_p} \langle \mathcal{H}(\mathbf{v}) \rangle. \quad (3.13)$$

If one can prove that

$$\mathcal{H}(\mathbf{v}) + \gamma \geq 0 \quad \forall \mathbf{v} \quad (3.14)$$

for a background flow \mathbf{U} and some constant γ , then we have the following bound on the flow rate

$$Q \geq 2 \int_{\phi=0}^{2\pi} \int_{r=0}^1 U_s r \, dr \, d\phi - \frac{1}{s_p Re} \|\nabla \mathbf{U}\|_2^2 - \frac{2\gamma}{s_p}. \quad (3.15)$$

Following the convention (Doering & Constantin 1994; Constantin & Doering 1995), we call (3.14) the spectral constraint.

Note that the background method formulation given in Constantin & Doering (1995) for pressure-driven channel flows assumes that the background flow \mathbf{U} is unidirectional and planar (a choice that is only suitable for planar geometries). As a result, the term II in (3.7) is zero and therefore the functional $\mathcal{H}(\mathbf{v})$ is homogenous in their work. Here, we have given the background method formulation for a general background flow \mathbf{U} . Also, as we shall see, the choice of the background flow which works in the present case, is two-dimensional which leads to a nonzero term II in (3.7) and therefore the resultant functional $\mathcal{H}(\mathbf{v})$ is inhomogenous.

4. Bounds on flow rate and friction factor

In this section, we obtain a lower bound on the flow rate and an equivalent upper bound on the friction factor. We choose a family of background flows with varying boundary layer thickness along the circumference of the pipe. This variation of the boundary layer thickness will be carefully selected so that the spectral constraint (3.14) is satisfied while

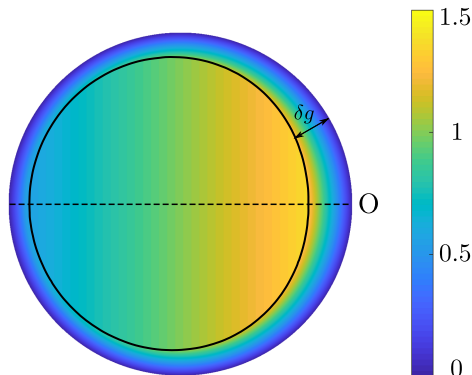


Figure 2: Variation of the streamwise component U_s of the background flow (4.1) across a cross-section of the pipe. In this example, the pipe's curvature is $\kappa = 0.5$ and torsion is $\tau = 0.25$. The solid black curve shows the edge of the boundary layer with variable thickness $\delta g(s, \phi)$. The point O denotes the outer edge of the pipe, i.e., the point on the cross-section, which is farthest from the axis of rotation of the helical pipe. The background flow in this figure corresponds to $\Lambda = 1$, and the boundary layer shape $g(s, \phi)$ is given by (4.21), which is the shape obtained in the process of optimizing the bound.

optimizing the bound (3.15) simultaneously for different values of curvature κ and torsion τ , thereby obtaining a geometrical dependence on these parameters. Note that in this paper, the *boundary layer* refers to the term boundary layer used in the context of the background method (see for instance, Doering & Constantin 1994; Goluskin & Doering 2016) and is not the conventional viscous boundary layer.

4.1. Choice of background flow

We make the following choice of background flow

$$U(s, r, \phi) = \begin{cases} (\Lambda(1 - r\kappa \cos(\phi - \tau s)), 0, \Lambda\tau r) & \text{if } 0 \leq r < 1 - \delta g(s, \phi) \\ \left(\Lambda(1 - r\kappa \cos(\phi - \tau s)) \left(\frac{1-r}{\delta g(s, \phi)} \right), 0, \Lambda\tau r \left(\frac{1-r}{\delta g(s, \phi)} \right) \right) & \text{if } 1 - \delta g(s, \phi) \leq r \leq 1. \end{cases} \quad (4.1)$$

Here, Λ is a constant that will be adjusted later to optimize the bound,

$$\delta = \frac{1}{Re}, \quad (4.2)$$

and $g(s, \phi)$ is a non-zero bounded differentiable function of s and ϕ , that satisfies

$$0 < g_l \leq g(s, \phi) \leq g_u \quad \text{and} \quad \left| \frac{\partial g}{\partial s} \right|, \left| \frac{\partial g}{\partial \phi} \right| \leq g'_u \quad \forall s \in [0, s_p], \phi \in [0, 2\pi], \quad (4.3)$$

where g_l , g_u , and g'_u are constants independent of Re . The region $1 - \delta g(s, \phi) \leq r \leq 1$ is the boundary layer denoted as

$$\Omega_\delta = \{(s, r, \phi) | s \in [0, s_p], \phi \in [0, 2\pi], 1 - \delta g(s, \phi) \leq r \leq 1\}, \quad (4.4)$$

and the function $g(s, \phi)$ represents the shape of the boundary layer which will be determined later as part of the analysis to optimize the bound. Physically, (4.3) means that the thickness of the boundary layer is everywhere non-zero and finite, and it

varies smoothly. Figure (2) shows a color map of the streamwise component U_s of the background flow (4.1). It can be easily verified that the background flow field (4.1) satisfies the no-slip and impermeable boundary conditions on the pipe surface. Meanwhile, the divergence-free condition on the background flow enforces

$$g(s, \phi) = g(\phi - \tau s), \quad (4.5)$$

which constrains the choice of g . See Appendix A for the calculation of divergence of a vector in the (s, r, ϕ) coordinate system. Also, note that for this choice of \mathbf{U} , in the bulk region ($0 \leq r \leq 1 - \delta g(s, \phi)$), we have

$$\nabla \mathbf{U}_{\text{sym}} = \mathbf{0} \quad (4.6)$$

(see Appendix C) the reason being is that in this region \mathbf{U} is really a rigid body flow as viewed from some inertial frame of reference (see §5 Discussion and Concluding Remarks). Although we can obtain a bound on the flow rate with a constant boundary layer thickness, this choice does not provide the optimal bound as a function of the pipe's curvature κ and torsion τ . Unlike the case of planar geometries, the choice of the background flow (4.1) is not uniform in the bulk region. As can be seen in figure (2), the magnitude of the streamwise component U_s of the background flow in the bulk region varies and is higher towards the outer edge O of the pipe than the inner edge. As such, a constant boundary layer thickness is not necessarily the optimal choice for every κ and τ . Therefore, it is natural to choose a variable boundary layer thickness (which is more general than the choice of constant boundary layer thickness) since our goal is to optimize bounds simultaneously for different curvature and torsion. Furthermore, in the process of obtaining bounds, we complement this choice of variable boundary layer thickness with inequalities suitably constructed (from standard analysis inequalities) to achieve this goal. In the forthcoming analysis, we will be interested in obtaining a bound in the limit of high Reynolds number and therefore will be frequently making use of the fact that $Re \gg 1$ or $\delta \ll 1$ to retain only the leading order terms.

4.2. The spectral constraint

In this subsection, we use analysis techniques to obtain a condition under which the spectral constraint (3.14) is satisfied. In what follows, we shall make use of a crucial inequality, whose proof is given in Appendix B.

INEQUALITY 1. *Let $w : \Omega_\delta \rightarrow \mathbb{R}$ be a square integrable function such that $w(s, 1, \phi) = 0$ for all $0 \leq s \leq s_p$ and $0 \leq \theta \leq 2\pi$, then the following statement is true*

$$\int_{\Omega_\delta} \sigma w^2 \, d\mathbf{x} \leq \frac{\delta^2}{2} \int_{\Omega_\delta} \sigma(s, 1, \phi) g^2(s, \phi) \left(\frac{\partial w}{\partial r} \right)^2 \, d\mathbf{x} + O(\delta^3) \|\nabla w\|_2^2. \quad (4.7)$$

Here, $\sigma : \Omega_\delta \rightarrow \mathbb{R}$ is a positive bounded $O(1)$ function that satisfies

$$|\sigma(s, r, \phi) - \sigma(s, 1, \phi)| = O(\delta) \quad \text{for } (s, r, \phi) \in \Omega_\delta. \quad (4.8)$$

For convenience, we make use of the big O notation $O(\cdot)$. Let m and n be two functions, then in this notation, writing $m(\delta) = O(n(\delta))$ means that there exists two positive constants $C > 0$ and $\delta_0 > 0$ such that $|m(\delta)| \leq C|n(\delta)|$ whenever $0 \leq \delta < \delta_0$.

We start by obtaining a bound on I as defined in (3.7). Making use of (4.6) leads to

$$I = \int_{\Omega} (\mathbf{v} \cdot \nabla \mathbf{U}_{\text{sym}}) \cdot \mathbf{v} \, d\mathbf{x} = \int_{\Omega_\delta} (\mathbf{v} \cdot \nabla \mathbf{U}_{\text{sym}}) \cdot \mathbf{v} \, d\mathbf{x}. \quad (4.9)$$

The following inequality is obtained by substituting $\nabla \mathbf{U}_{\text{sym}}$ (use (C2) from Appendix C for the calculation of $\nabla \mathbf{U}_{\text{sym}}$) into (4.9)

$$\begin{aligned}
 |I| \leq & \int_{\Omega_\delta} \xi_1(s, r, \phi) |v_s| |v_r| \, d\mathbf{x} + \int_{\Omega_\delta} \xi_2(s, r, \phi) |v_\phi| |v_r| \, d\mathbf{x} \\
 & + \int_{\Omega_\delta} \xi_3 v_s^2 \, d\mathbf{x} + \int_{\Omega_\delta} \xi_4 v_\phi^2 \, d\mathbf{x} + \int_{\Omega_\delta} \xi_5 |v_s| |v_\phi| \, d\mathbf{x}, \quad (4.10)
 \end{aligned}$$

where

$$\begin{aligned}
 \xi_1(s, r, \phi) &= \frac{\Lambda(1 - r\kappa \cos(\phi - \tau s))}{\delta g}, & \xi_2(s, r, \phi) &= \frac{\Lambda \tau r}{\delta g}, \\
 \xi_3 &= \max_{(s, r, \phi) \in \Omega_\delta} \frac{\Lambda(1 - r)}{\delta g^2} \left| \frac{\partial g}{\partial s} \right|, & \xi_4 &= \max_{(s, r, \phi) \in \Omega_\delta} \frac{\Lambda \tau (1 - r)}{\delta g^2} \left| \frac{\partial g}{\partial \phi} \right|, \\
 \xi_5 &= \max_{(s, r, \phi) \in \Omega_\delta} \frac{\Lambda(1 - r)}{\delta g^2} \left[\frac{\tau r}{(1 - r\kappa \cos(\phi - \tau s))} \left| \frac{\partial g}{\partial s} \right| + \frac{(1 - r\kappa \cos(\phi - \tau s))}{r} \left| \frac{\partial g}{\partial \phi} \right| \right]. \quad (4.11)
 \end{aligned}$$

Given that $1 - r$ is $O(\delta)$ in the boundary layer, and using the constraints on g and its derivatives from (4.3), implies that ξ_3 , ξ_4 , and ξ_5 are $O(1)$ constants. Using Young's inequality $|v_s| |v_\phi| \leq (|v_s|^2 + |v_\phi|^2)/2$, the last three integrals in (4.10) can be replaced by

$$\int_{\Omega_\delta} \left(\xi_3 + \frac{\xi_5}{2} \right) v_s^2 \, d\mathbf{x} + \int_{\Omega_\delta} \left(\xi_4 + \frac{\xi_5}{2} \right) v_\phi^2 \, d\mathbf{x}. \quad (4.12)$$

An application of Inequality 1 to these two integrals with $w = v_s$ in the first integral, $w = v_\phi$ in the second integral and taking σ to be an $O(1)$ constant in both cases results a bound on I as

$$|I| \leq \int_{\Omega_\delta} \xi_1(s, r, \phi) |v_s| |v_r| \, d\mathbf{x} + \int_{\Omega_\delta} \xi_2(s, r, \phi) |v_\phi| |v_r| \, d\mathbf{x} + O(\delta^2) \|\nabla \mathbf{v}\|_2^2. \quad (4.13)$$

In a similar manner, we obtain bounds on the remaining two integrals in (4.13). These bounds contribute to the leading order term of the bound on $|I|$; therefore, this time we perform the computation wisely with the intent of optimizing the bound on $|I|$ simultaneously in κ and τ . Using the following inequalities (based on Young's inequality) in (4.13)

$$|v_s| |v_r| \leq \frac{c_1(s, \phi) |v_s|^2}{2} + \frac{|v_r|^2}{2c_1(s, \phi)}, \quad |v_\phi| |v_r| \leq \frac{c_2(s, \phi) |v_\phi|^2}{2} + \frac{|v_r|^2}{2c_2(s, \phi)}, \quad (4.14)$$

where

$$0 < c_1(s, \phi) \quad \text{and} \quad 0 < c_2(s, \phi), \quad (4.15)$$

results in

$$\begin{aligned}
 |I| \leq & \int_{\Omega_\delta} \left[\frac{c_1(s, \phi) \xi_1(s, r, \phi)}{2} \right] |v_s|^2 \, d\mathbf{x} + \int_{\Omega_\delta} \left[\frac{\xi_1(s, r, \phi)}{2c_1(s, \phi)} + \frac{\xi_2(s, r, \phi)}{2c_2(s, \phi)} \right] |v_r|^2 \, d\mathbf{x} \\
 & + \int_{\Omega_\delta} \left[\frac{c_2(s, \phi) \xi_2(s, r, \phi)}{2} \right] |v_\phi|^2 \, d\mathbf{x} + O(\delta^2) \|\nabla \mathbf{v}\|_2^2. \quad (4.16)
 \end{aligned}$$

We apply the Inequality 1 to the three integrals in (4.16) with $w = v_s, v_r$, and v_ϕ and

taking σ to be the corresponding terms in the square brackets times δ , which results in

$$|I| \leq \frac{\Lambda\delta}{4} \left[\int_{\Omega_\delta} p_1 \left(\frac{\partial v_s}{\partial r} \right)^2 d\mathbf{x} + \int_{\Omega_\delta} p_2 \left(\frac{\partial v_r}{\partial r} \right)^2 d\mathbf{x} + \int_{\Omega_\delta} p_3 \left(\frac{\partial v_\phi}{\partial r} \right)^2 d\mathbf{x} \right] + O(\delta^2) \|\nabla \mathbf{v}\|_2^2, \quad (4.17)$$

where

$$\begin{aligned} p_1 &= (1 - \kappa \cos(\phi - \tau s))g(s, \phi)c_1(s, \phi), \\ p_2 &= \frac{(1 - \kappa \cos(\phi - \tau s))g(s, \phi)}{c_1(s, \phi)} + \frac{\tau g(s, \phi)}{c_2(s, \phi)}, \\ p_3 &= \tau g(s, \phi)c_2(s, \phi). \end{aligned} \quad (4.18)$$

We now choose the functions $g(s, \phi)$, $c_1(s, \phi)$, and $c_2(s, \phi)$ so that p_1 , p_2 , and p_3 are constants. For this choice, the bound on I can be written as

$$|I| \leq \frac{\Lambda\delta}{4} \max\{p_1, p_2, p_3\} \|\nabla \mathbf{v}\|_2^2 + O(\delta^2) \|\nabla \mathbf{v}\|_2^2. \quad (4.19)$$

To optimize the bound, we need

$$p_1 = p_2 = p_3, \quad (4.20)$$

as shown in Appendix C. Combining this condition with the requirement that p_1, p_2 , and p_3 should be constants leads to

$$\begin{aligned} g(s, \phi) &= \frac{g_c}{\sqrt{(1 - \kappa \cos(\phi - \tau s))^2 + \tau^2}} \\ c_1(s, \phi) &= \sqrt{1 + \frac{\tau^2}{(1 - \kappa \cos(\phi - \tau s))^2}}, \quad c_2(s, \phi) = \sqrt{1 + \frac{(1 - \kappa \cos(\phi - \tau s))^2}{\tau^2}} \end{aligned} \quad (4.21)$$

with g_c being an $O(1)$ positive constant. Note that the function $g(s, \phi)$ satisfies the constraints (4.3) and (4.5), where the constants g_l, g_u, g'_u in (4.3) can be chosen as

$$g_l = \frac{g_c}{\sqrt{(1 + \kappa)^2 + \tau^2}}, \quad g_u = \frac{g_c}{\sqrt{(1 - \kappa)^2 + \tau^2}}, \quad \text{and } g'_u = \frac{2g_c}{[(1 - \kappa)^2 + \tau^2]^{3/2}}. \quad (4.22)$$

Combining (4.18), (4.19), and (4.21) gives a bound on I as

$$|I| \leq \left| \int_{\Omega} \mathbf{v} \cdot \nabla \mathbf{U} \cdot \mathbf{v} d\mathbf{x} \right| \leq \left(\frac{\Lambda g_c \delta}{4} + O(\delta^2) \right) \|\nabla \mathbf{v}\|_2^2. \quad (4.23)$$

Next, we show that the contribution of term II , as defined in (3.7), is of higher order in δ compared to term I . First note that for any scalar function Ψ

$$II = \int_{\Omega} \mathbf{U} \cdot \nabla \mathbf{U} \cdot \mathbf{v} d\mathbf{x} = \int_{\Omega} (\mathbf{U} \cdot \nabla \mathbf{U} - \nabla \Psi) \cdot \mathbf{v} d\mathbf{x} \quad (4.24)$$

using the incompressibility of \mathbf{v} , together with the fact that \mathbf{v} satisfies the homogenous boundary conditions. Then, if we choose Ψ such that $\mathbf{U} \cdot \nabla \mathbf{U} = \nabla \Psi$ in $\Omega \setminus \Omega_\delta$, namely,

$$\Psi(s, r, \phi) = \Lambda^2 \kappa \cos(\phi - \tau s) \left(r - \frac{r^2}{2} \kappa \cos(\phi - \tau s) \right) - \frac{\Lambda^2 \tau^2 r^2}{2}, \quad (4.25)$$

then one can readily check that

$$|(\mathbf{U} \cdot \nabla \mathbf{U} - \nabla \Psi)|(\mathbf{x}) = \begin{cases} 0 & \text{if } \mathbf{x} \in \Omega \setminus \Omega_\delta \\ O(1) & \text{if } \mathbf{x} \in \Omega_\delta \end{cases}. \quad (4.26)$$

See Appendix C for the calculation of $\nabla \mathbf{U}$. Using (4.26), we can finally obtain a bound on II as

$$\begin{aligned}
 |II| &= \left| \int_{\Omega} \mathbf{U} \cdot \nabla \mathbf{U} \cdot \mathbf{v} \, d\mathbf{x} \right| = \left| \int_{\Omega} (\mathbf{U} \cdot \nabla \mathbf{U} - \nabla \Psi) \cdot \mathbf{v} \, d\mathbf{x} \right| \\
 \implies |II| &\leq O(1) \int_{\Omega_{\delta}} |\mathbf{v}| \, d\mathbf{x} \\
 &\leq O(1) \int_{\Omega_{\delta}} |\mathbf{v}|^2 \, d\mathbf{x} + O(1) \int_{\Omega_{\delta}} 1 \, d\mathbf{x} \\
 &\leq O(\delta^2) \|\nabla \mathbf{v}\|_2^2 + s_p O(\delta).
 \end{aligned} \tag{4.27}$$

We have used Young's inequality to obtain the third line and Inequality 1 to obtain the last line. Finally, we obtain a bound on $\mathcal{H}(\mathbf{v})$ defined in (3.7) using the triangle inequality and the bounds derived on I and II as

$$\mathcal{H}(\mathbf{v}) \geq \frac{1}{2Re} \|\nabla \mathbf{v}\|_2^2 - \left(\frac{\Lambda g_c \delta}{4} + O(\delta^2) \right) \|\nabla \mathbf{v}\|_2^2 - s_p O(\delta), \tag{4.28}$$

which implies

$$\mathcal{H}(\mathbf{v}) + \gamma \geq 0 \tag{4.29}$$

as long as

$$g_c \leq \frac{2}{\Lambda} + O(\delta) \quad \text{and} \quad \gamma = s_p O(\delta). \tag{4.30}$$

4.3. Bound on mean quantities

We are now ready to compute the bound on the flow rate. We begin by evaluating the first term on the right-hand-side of (3.15) as

$$\begin{aligned}
 \int_{\phi=0}^{2\pi} \int_{r=0}^1 U_s r \, dr \, d\phi &= \int_{\phi=0}^{2\pi} \int_{r=0}^{1-\delta g(s,\phi)} \Lambda (1 - r\kappa \cos(\phi - \tau s)) r \, dr \, d\phi \\
 &\quad + \int_{\phi=0}^{2\pi} \int_{1-\delta g(s,\phi)}^1 \Lambda (1 - r\kappa \cos(\phi - \tau s)) \frac{(1-r)}{\delta g} r \, dr \, d\phi \\
 &= \int_{\phi=0}^{2\pi} \int_{r=0}^1 \Lambda (1 - r\kappa \cos(\phi - \tau s)) r \, dr \, d\phi + O(\delta) \\
 &= \pi \Lambda + O(\delta).
 \end{aligned} \tag{4.31}$$

Similarly, the second term on the right-hand-side of (3.15) is as follows

$$\begin{aligned}
 \|\nabla \mathbf{U}\|_2^2 &= \int_{\Omega_{\delta}} |\nabla \mathbf{U}|^2 \, d\mathbf{x} + \int_{\Omega \setminus \Omega_{\delta}} |\nabla \mathbf{U}|^2 \, d\mathbf{x} \\
 &= \int_{s=0}^{s_p} \int_{\phi=0}^{2\pi} \int_{1-\delta g(s,\phi)}^1 |\nabla \mathbf{U}|^2 h_s h_r h_{\phi} \, dr \, d\phi \, ds + s_p O(1) \\
 &= \frac{2\pi \Lambda^2 s_p}{\delta g_c} I(\kappa, \tau) + s_p O(1),
 \end{aligned} \tag{4.32}$$

where

$$I(\kappa, \tau) = \frac{1}{2\pi} \int_0^{2\pi} \left((1 - \kappa \cos \alpha)^2 + \tau^2 \right)^{3/2} (1 - \kappa \cos \alpha) \, d\alpha. \tag{4.33}$$

Pipe	Flow rate Q (lower bound)	Friction factor λ (upper bound)
Straight	\mathcal{C}	\mathcal{D}
Helical	$\mathcal{C}/\sqrt{I(\kappa, \tau)}$	$\mathcal{D}I(\kappa, \tau)$
Toroidal	$\mathcal{C} \left(1 + 3\kappa^2 + \frac{3}{8}\kappa^4\right)^{-\frac{1}{2}}$	$\mathcal{D} \left(1 + 3\kappa^2 + \frac{3}{8}\kappa^4\right)$
Helical ($\tau \ll 1$)	$\mathcal{C} \left(1 + 3\kappa^2 + \frac{3}{8}\kappa^4\right)^{-\frac{1}{2}} \left(1 - \frac{3(2+\kappa^2)\tau^2}{8+24\kappa^2+3\kappa^4}\right)$	$\mathcal{D} \left(1 + 3\kappa^2 + \frac{3}{8}\kappa^4\right) \left(1 + \frac{6(2+\kappa^2)\tau^2}{8+24\kappa^2+3\kappa^4}\right)$

Table 1: The first column shows the pipe type, the second column shows the lower bound on the flow rate Q (4.38) and the third column shows the upper bound on the friction factor λ (4.39) in different limits of curvature κ and torsion τ . In the table $\mathcal{C} = (32\pi^2/27)^{\frac{1}{2}}$ and $\mathcal{D} = 27/8$.

The integrand in the second line of (4.32) is explicitly calculated in (C 4), see Appendix C. Using (4.31) and (4.32) in (3.15), we obtain a bound on the flow rate Q as

$$Q \geq 2\pi\Lambda - \frac{2\pi\Lambda^2}{g_c}I(\kappa, \tau) + O(\delta). \quad (4.34)$$

We see that choosing a small value of g_c will make the bound on Q worse. Therefore, to obtain the best possible bound, we choose the largest possible value of g_c which satisfies the constraint (4.30), i.e.,

$$g_c = \frac{2}{\Lambda} + O(\delta). \quad (4.35)$$

The bound on Q then reads

$$Q \geq 2\pi\Lambda - \pi\Lambda^3I(\kappa, \tau) + O(\delta). \quad (4.36)$$

All that remains is to choose Λ to maximize this lower bound. The optimal value of Λ is given by

$$\Lambda = \sqrt{\frac{2}{3I(\kappa, \tau)}}. \quad (4.37)$$

Substituting (4.37) into (4.36) and using $\delta = 1/Re$ as defined earlier in (4.2), gives a bound on the flow rate as

$$Q \geq \sqrt{\frac{32\pi^2}{27I(\kappa, \tau)}} + O(Re^{-1}). \quad (4.38)$$

Using this lower bound, together with the definition (2.20) of the friction factor λ in terms of Q , we finally obtain an upper bound on the friction factor as

$$\lambda \leq \lambda_b = \frac{27}{8}I(\kappa, \tau) + O(Re^{-1}). \quad (4.39)$$

These bounds on the flow rate (4.38) and friction factor (4.39) are also valid for a toroidal ($\kappa \neq 0, \tau = 0$) or a straight ($\kappa = 0, \tau = 0$) pipe. In general, the integral $I(\kappa, \tau)$ cannot be obtained analytically except when τ is zero or small. Table 1 summarizes the bounds derived on the flow rate and friction factor in different limits of curvature and torsion. For a toroidal pipe, a small radius of curvature has a second-order effect on the bounds (see table 1), which is also the case in the exact solution for the flow at

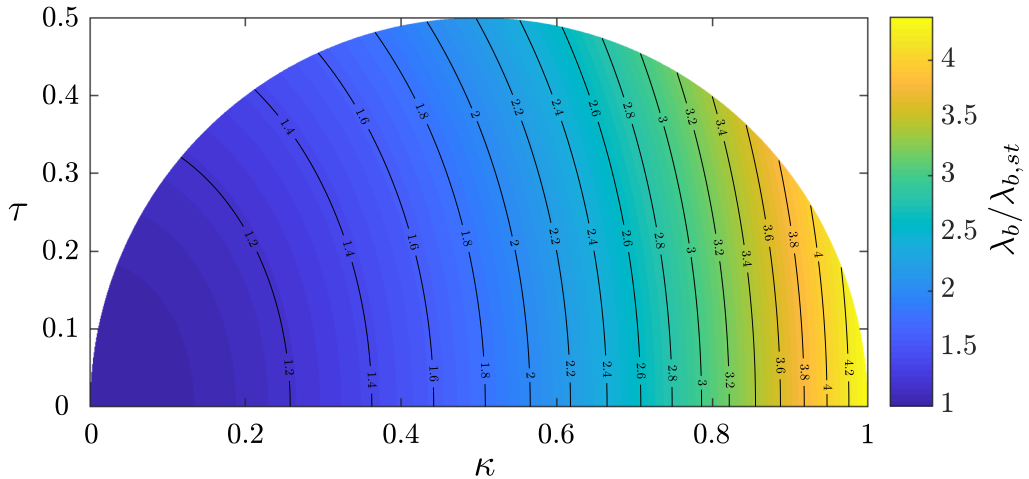


Figure 3: Ratio of the bound on the friction factor for a helical pipe as compared to a straight pipe ($\lambda_b/\lambda_{b,st}$), as a function of curvature κ and torsion τ . Here, λ_b is given by (4.39) and $\lambda_{b,st} = 27/8$.

low Reynolds number (see Dean 1928). Similarly, for a helical pipe, the effect of a small torsion is of second-order on our bounds, and as before, this is the case for the steady-state solution at low Reynolds number (see Tuttle 1990). More generally, the effect of increasing curvature and torsion is always to decrease the lower bound on the volume flow rate and to increase the upper bound on the friction factor. For a straight pipe, the bound on the friction factor reduces to $\lambda_{b,st} = 27/8$ which is 12.5 times larger than the bound 0.27 (Plasting & Kerswell 2005) obtained by solving the variational problem numerically. Figures 3 and 4 show a color map of the ratio of the bound on the friction factor for a helical pipe λ_b to the bound on the friction factor $\lambda_{b,st}$ for a straight pipe, as a function of κ, τ (figure 3) and a, b (figure 4). To avoid a self-intersecting geometry, we restrict to $1 < a < \infty$ and $0 \leq b < \infty$, which corresponds to a semicircular region in κ, τ space (see figure 3). The maximum increase in the bound on the friction factor is when the pipe approaches a horn torus ($\kappa = 1, \tau = 0$), which is a factor $35/8 = 4.375$ larger than for the straight pipe. From figure 4, we see that with the increase of the non-dimensional helix radius a or pitch $2\pi b$, the bound on the friction factor approaches that of a straight pipe, as expected.

5. Discussion and Concluding Remarks

In this paper, we used the background method to obtain bounds on the flow rate and friction factor in helical pipe flows. The bounds that we obtained are also valid for toroidal and straight pipes as limiting cases. By choosing a boundary layer whose thickness varies along the circumference of the pipe, we were able to obtain these bounds as a function of pipe geometry. In particular, we found that the bound on the friction factor varies with curvature κ and torsion τ according to the integral $I(\kappa, \tau)$, defined in (4.33), whose value is one for the straight pipe, i.e. $I(0, 0) = 1$.

The bound that we obtained on the friction factor is independent of the Reynolds number. However, it is a known property of wall-bounded flows in smooth geometries that the friction factor decreases as $(\log Re)^2$, as predicted using the logarithmic friction law (Tennekes & Lumley 1972). Therefore, it appears that our bound, in terms of Reynolds

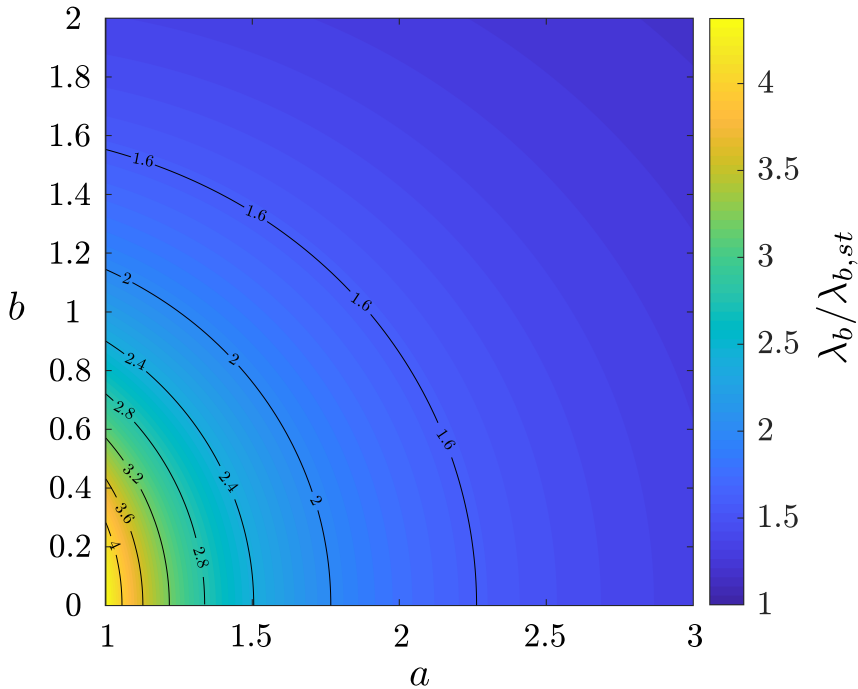


Figure 4: Ratio of the bound on the friction factor for a helical pipe as compared to a straight pipe ($\lambda_b/\lambda_{b,st}$), as a function of the non-dimensional geometric parameters a and b as defined earlier.

number scaling is off by factor of $(\log Re)^2$, a situation similar to previous applications of the background method to shear and pressure-driven flows (Doering & Constantin 1992, 1994; Constantin & Doering 1995; Plasting & Kerswell 2003). Despite being unable to capture the correct scaling in terms of Reynolds number, one may ask whether the geometrical scaling $I(\kappa, \tau)$ in the bound on the friction factor (4.39) correctly captures the variation of λ on the pipe geometry, as observed in the experiments. Assuming that is the case, then one would expect that the experimental data for the friction factor (λ_{exp}), when scaled with the integral $I(\kappa, \tau)$, should only be a function of the Reynolds number. Here, we test this hypothesis on data from carefully conducted experiments by Cioncolini & Santini (2006) for flows in helical pipes with negligible torsion. The results are shown in figure 5. In reporting these results, we have used the Reynolds number based on the pipe diameter ($Re_D = 2Re$), to be consistent with the literature. From figure 5, we see that our scaling, being second-order in the curvature κ , has a negligible effect on the pipes with small curvature ratios $\kappa = 0.028, 0.042, 0.059$. As such, the rescaled data $\lambda_{exp}/I(\kappa, \tau)$ looks almost identical to the original data, and does not collapse on a universal curve, contrary to our expectation. It thus appears that, for the range of Reynolds number considered in figure 5, the curvature has a first-order effect on the friction factor in the experiments, as opposed to the second-order effect predicted by our bound (see table 1). On a more positive note, the effect becomes qualitatively noticeable for $\kappa = 0.143$, and the rescaled data is more compact than the original data, suggesting that the dependence on the curvature κ given by the scaling $I(\kappa, \tau)$ at least has the right sign.

There could be several possible reasons for the discrepancy between the data and the

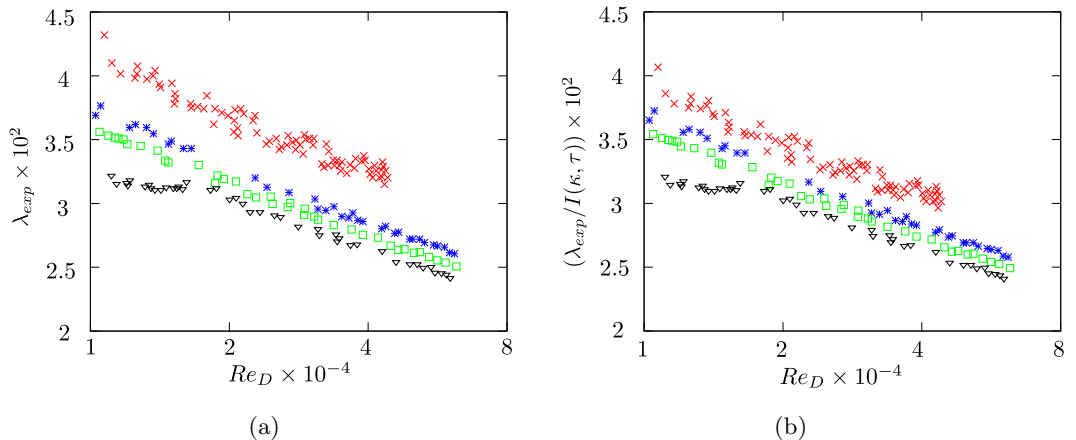


Figure 5: (a) Data from Cioncolini & Santini (2006), showing the friction factor (λ_{exp}) as a function of Reynolds number for four different helical pipes: (i) $\kappa = 0.028$, $\tau = 0.49 \times 10^{-3}$ (∇), (ii) $\kappa = 0.042$, $\tau = 1.87 \times 10^{-3}$ (\square), (iii) $\kappa = 0.059$, $\tau = 2.97 \times 10^{-3}$ ($*$), and (iv) $\kappa = 0.143$, $\tau = 11.4 \times 10^{-3}$ (\times). (b) Scaled friction factor ($\lambda_{exp}/I(\kappa, \tau)$) as a function of Reynolds number for the same four helical pipes.

theoretical bound. First, there is further improvement possible in our analysis to capture the geometrical dependence of the friction factor better. One way to find that out would be to compute numerically the optimal bound on, e.g. the friction factor, similar to other studies of the background method (Plasting & Kerswell 2003; Wen *et al.* 2013, 2015; Fantuzzi & Wynn 2015, 2016; Fantuzzi 2018; Tilgner 2017, 2019) and then see if this optimal bound better accounts for the experimental data. The second possible reason for the discrepancy is that the Reynolds numbers achieved in the experiments are not high enough for our scalings to apply yet. Indeed, the critical Reynolds number for instability for a torus with curvature ratio $\kappa \approx 0.1$ is $Re_{D,c} \approx 3500$ (Canton *et al.* 2016), which is higher than that of a straight pipe $Re_{D,c} \approx 2040$ (Avila *et al.* 2011). Also, the transition for $\kappa \gtrsim 0.028$ is supercritical (Kühnen *et al.* 2015), suggesting that the flow structure slowly becomes more complex with increasing Reynolds number, only becoming fully developed turbulence at much higher Reynolds number. As a result, we believe that the maximum Reynolds number achieved by Cioncolini & Santini (2006) ($Re_D \approx 6 \times 10^4$), may not be high enough for our scalings to apply.

Beyond the fact that the bounds and the data do not agree as well as we could have hoped for, the technique used in this paper to derive formal bounds for such complex geometry deserves to be discussed. The feasibility of the background method relies on the existence of a divergence-free background flow field \mathbf{U} , which satisfies the same boundary conditions as the full flow \mathbf{u} and for which $\mathcal{H}(\mathbf{v}) + \gamma$ is positive semi-definite, i.e. the spectral constraint (3.14) is satisfied. The situation becomes particularly difficult at high Reynolds number when the only undoubtedly positive term in $\mathcal{H}(\mathbf{v})$ (see term *III* in equation 3.7) becomes small. However, for an $O(1)$ background flow \mathbf{U} for which $\nabla \mathbf{U}_{\text{sym}}$ is zero in bulk and is of $O(\delta^{-1})$ in a $O(\delta)$ thick boundary layer near the surface, it is possible to show that $\mathcal{H}(\mathbf{v}) + \gamma$ is positive semi-definite, as done in the present study and in several other studies of the background method (Doering & Constantin 1994; Marchioro 1994; Constantin & Doering 1995; Wang 1997). One may therefore generally ask under which circumstances can such a background flow \mathbf{U} exist. We start by making

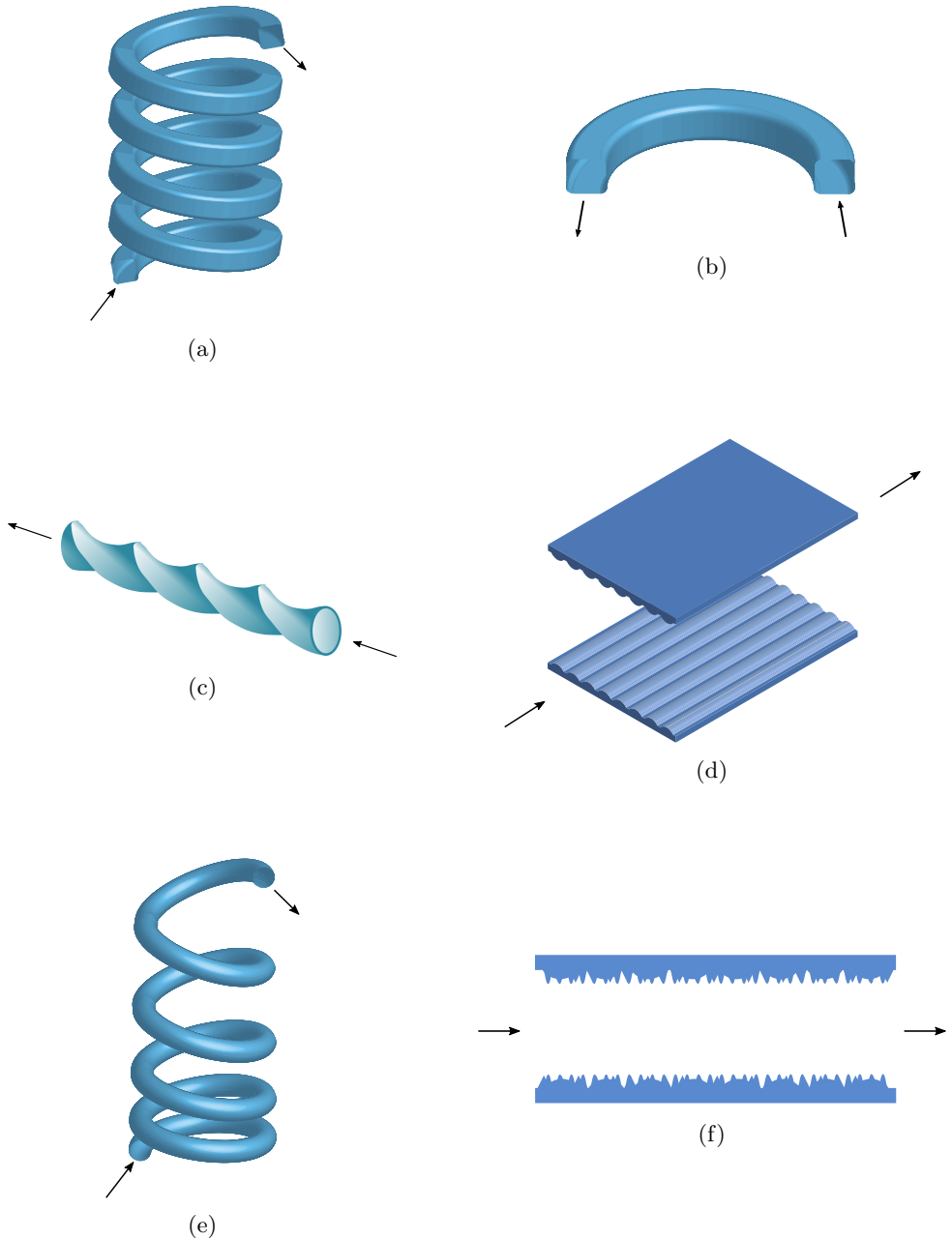


Figure 6: Pressure driven flow (a) through a helical pipe with a square cross-section, (b) through a toroidal pipe with a square cross-section, (c) through an axially twisted pipe with an elliptical cross-section, (d) between grooved walls where the grooves are aligned in the direction of the pressure gradient, (e) through a helical pipe with varying pitch, and (f) between rough walls (two-dimensional view). Arrows indicate the direction of the mean flow.

two observations. First, that an $O(1)$ change in the velocity field in a boundary layer of thickness δ leads to $|\nabla \mathbf{U}_{\text{sym}}| = O(\delta^{-1})$ in the boundary layer. Second, that a divergence-free flow field \mathbf{V} for which $\nabla \mathbf{V}_{\text{sym}} = \mathbf{0}$ is given by

$$\mathbf{V}(\mathbf{x}) = \mathbf{A}\mathbf{x} + \mathbf{V}_0, \quad (5.1)$$

where \mathbf{A} is a constant skew-symmetric tensor and \mathbf{V}_0 is a constant velocity field. The flows given by (5.1) include uniform flow, and rigid body flow. These two observations tell us that for a problem with prescribed tangential-velocity boundary conditions at impermeable boundaries where the boundaries have the shape of streamtubes of the flow field given by (5.1), it is always possible to find a background flow \mathbf{U} for which $\nabla \mathbf{U}_{\text{sym}} = \mathbf{0}$ in the bulk and is $O(\delta^{-1})$ in a $O(\delta)$ thick boundary layer near the surface. Indeed, this is done by choosing $\mathbf{U} = \mathbf{V}$ in the bulk and by adjusting the tangential component of \mathbf{U} by an $O(1)$ in the $O(\delta)$ boundary layer to satisfy the prescribed tangential-velocity boundary conditions. Note that these arguments apply to both pressure-driven flow and surface-velocity-driven flow problems, as they both involve the same spectral constraint (3.7). Wang (1997) considered the general problem of bounding the energy dissipation for a flow driven by an imposed tangential velocity at the boundaries in an arbitrary bounded domain when $\mathbf{A} = \mathbf{0}$ and $\mathbf{V}_0 = \mathbf{0}$. Considering the more general cases where \mathbf{A} and \mathbf{V}_0 are non-zero enables us to extend the class of problems, as demonstrated in this paper.

Figure 6 shows some examples of pressure-driven flows where the criterion mentioned in the last paragraph can or cannot be applied. Although we considered the cross-section of the pipe to be circular in this paper, in general, a bound can be obtained on the friction factor for a helical, toroidal, or a straight pipe of any cross-section. Figure 6a and figure 6b, for example, show a helical pipe and a toroidal pipe with a square cross-section. These two cases fall under the case when $\mathbf{A} \neq \mathbf{0}, \mathbf{V}_0 \neq \mathbf{0}$ and $\mathbf{A} \neq \mathbf{0}, \mathbf{V}_0 = \mathbf{0}$, respectively. Figure 6c shows a pressure-driven flow through an axially twisted pipe with an elliptical cross-section. According to the criterion mentioned in the last paragraph, the background method can be applied to this example with $\mathbf{A} \neq \mathbf{0}, \mathbf{V}_0 \neq \mathbf{0}$. Further, we can use the background method with $\mathbf{A} = \mathbf{0}, \mathbf{V}_0 \neq \mathbf{0}$ in case of pressure-driven flow between grooved walls (figure 6d) as long as the grooves are aligned in the direction of the pressure gradient. However, for pressure-driven flow through a helical pipe with varying pitch (figure 6e) or pressure-driven flow between rough walls (figure 6f), there is no choice of \mathbf{A} and \mathbf{V}_0 which works.

The criterion we have mentioned is, so far, a sufficient criterion for the applicability of the background method. Whether this criterion is also a necessary one remains to be determined. The answer to that question is fundamental since it would provide definite guidance about which problems can and cannot be tackled using the background method.

Acknowledgement

A.K. acknowledges the support from the Dean's fellowship and Regents' fellowship from the Baskin School of Engineering at UC Santa Cruz, from the GFD fellowship program 2019 at the Woods Hole Oceanographic Institution, and from NSF AST 1814327. Many thanks to P. Garaud and anonymous referees for providing useful comments, which helped to improve the quality of the paper.

Declaration of interests

The author reports no conflict of interest.

Appendix A. The (s, r, ϕ) coordinate system

An infinitesimal displacement $d\mathbf{x}$ in the (s, r, ϕ) coordinate system can be written as

$$d\mathbf{x} = h_s ds \mathbf{e}_s + h_r dr \mathbf{e}_r + h_\phi d\phi \mathbf{e}_\phi, \quad (\text{A } 1)$$

where the scale factors are

$$h_s = (1 - r\kappa \cos(\phi - \tau s)), \quad h_r = 1, \quad h_\phi = r. \quad (\text{A } 2)$$

The gradient of a scalar field Ψ in the (s, r, ϕ) coordinate system is given by

$$\nabla \Psi = \frac{1}{h_s} \frac{\partial \Psi}{\partial s} \mathbf{e}_s + \frac{1}{h_r} \frac{\partial \Psi}{\partial r} \mathbf{e}_r + \frac{1}{h_\phi} \frac{\partial \Psi}{\partial \phi} \mathbf{e}_\phi. \quad (\text{A } 3)$$

The divergence of a vector field $\mathbf{q} = (q_s, q_r, q_\phi)$ in the (s, r, ϕ) coordinate system is

$$\nabla \cdot \mathbf{q} = \frac{1}{h_s h_r h_\phi} \left[\frac{\partial h_r h_\phi q_s}{\partial s} + \frac{\partial h_\phi h_s q_r}{\partial r} + \frac{\partial h_s h_r q_\phi}{\partial \phi} \right]. \quad (\text{A } 4)$$

Finally, the gradient of a vector $\mathbf{q} = (q_s, q_r, q_\phi)$ in the (s, r, ϕ) coordinate system is written as

$$\begin{aligned} \nabla \mathbf{q} = & \left(\frac{1}{h_s} \frac{\partial q_s}{\partial s} + \frac{q_r}{h_s h_r} \frac{\partial h_s}{\partial r} + \frac{q_\phi}{h_s h_\phi} \frac{\partial h_s}{\partial \phi} \right) \mathbf{e}_s \mathbf{e}_s + \left(\frac{1}{h_s} \frac{\partial q_r}{\partial s} - \frac{q_s}{h_s h_r} \frac{\partial h_s}{\partial r} \right) \mathbf{e}_s \mathbf{e}_r \\ & + \left(\frac{1}{h_s} \frac{\partial q_\phi}{\partial s} - \frac{q_s}{h_s h_\phi} \frac{\partial h_s}{\partial \phi} \right) \mathbf{e}_s \mathbf{e}_\phi + \left(\frac{1}{h_r} \frac{\partial q_s}{\partial r} - \frac{q_r}{h_r h_s} \frac{\partial h_r}{\partial s} \right) \mathbf{e}_r \mathbf{e}_s \\ & + \left(\frac{1}{h_r} \frac{\partial q_r}{\partial r} + \frac{q_s}{h_r h_s} \frac{\partial h_r}{\partial s} + \frac{q_\phi}{h_r h_\phi} \frac{\partial h_r}{\partial \phi} \right) \mathbf{e}_r \mathbf{e}_r + \left(\frac{1}{h_r} \frac{\partial q_\phi}{\partial r} - \frac{q_r}{h_r h_\phi} \frac{\partial h_r}{\partial \phi} \right) \mathbf{e}_r \mathbf{e}_\phi \\ & + \left(\frac{1}{h_\phi} \frac{\partial q_s}{\partial \phi} - \frac{q_\phi}{h_\phi h_s} \frac{\partial h_\phi}{\partial s} \right) \mathbf{e}_\phi \mathbf{e}_s + \left(\frac{1}{h_\phi} \frac{\partial q_r}{\partial \phi} - \frac{q_\phi}{h_\phi h_r} \frac{\partial h_\phi}{\partial r} \right) \mathbf{e}_\phi \mathbf{e}_r \\ & + \left(\frac{1}{h_\phi} \frac{\partial q_\phi}{\partial \phi} + \frac{q_r}{h_\phi h_r} \frac{\partial h_\phi}{\partial r} + \frac{q_s}{h_\phi h_s} \frac{\partial h_\phi}{\partial s} \right) \mathbf{e}_\phi \mathbf{e}_\phi. \end{aligned} \quad (\text{A } 5)$$

Appendix B. A few useful inequalities

INEQUALITY 0. Let $w : [1 - \delta g(s, \phi), 1] \rightarrow \mathbb{R}$ be a square integrable function such that $w(1) = 0$, then the following inequality holds

$$w^2(r) \leq \left(\frac{1-r}{1-\kappa \cos(\phi - \tau s)} + O(\delta^2) \right) \int_{1-\delta g(s, \phi)}^1 \left(\frac{\partial w}{\partial r'} \right)^2 (1 - r' \kappa \cos(\phi - \tau s)) r' dr' \quad (\text{B } 1)$$

for given s , and ϕ . Here, $r \in [1 - \delta g(s, \phi), 1]$.

Proof. For $r \in [1 - \delta g(s, \phi), 1]$, using the fundamental theorem of calculus and the Cauchy-Schwarz inequality, the following inequality holds

$$\begin{aligned} w^2(r) &= \left| \int_1^r \frac{dw}{dr'} dr' \right|^2 \\ &\leq \left(\int_r^1 \frac{1}{(1 - r' \kappa \cos(\phi - \tau s)) r'} dr' \right) \left(\int_{1-\delta g(s, \phi)}^1 \left(\frac{dw}{dr'} \right)^2 (1 - r' \kappa \cos(\phi - \tau s)) r' dr' \right). \end{aligned} \quad (\text{B } 2)$$

As mentioned earlier, the curvature satisfies $\kappa < 1$ and since $r' \leq 1$ in the above expression, we have $(1 - r'\kappa \cos(\phi - \tau s)) < 1$. Therefore, the integrands in both integrals are positive. Finally, using the fact that

$$\left| \frac{1}{(1 - r'\kappa \cos(\phi - \tau s))r'} - \frac{1}{1 - \kappa \cos(\phi - \tau s)} \right| = O(\delta)$$

when $r' \in [1 - \delta g(s, \phi), 1]$ completes the proof. \square

INEQUALITY 1. *Let $w : \Omega_\delta \rightarrow \mathbb{R}$ be a square integrable function such that $w(s, 1, \phi) = 0$ for all $0 \leq s \leq s_p$ and $0 \leq \theta \leq 2\pi$, then the following statement is true*

$$\int_{\Omega_\delta} \sigma w^2 \, d\mathbf{x} \leq \frac{\delta^2}{2} \int_{\Omega_\delta} \sigma(s, 1, \phi) g^2(s, \phi) \left(\frac{\partial w}{\partial r} \right)^2 \, d\mathbf{x} + O(\delta^3) \|\nabla w\|_2^2. \quad (\text{B3})$$

Here, $\sigma : \Omega_\delta \rightarrow \mathbb{R}$ is a positive bounded $O(1)$ function that satisfies

$$|\sigma(s, r, \phi) - \sigma(s, 1, \phi)| = O(\delta) \quad \text{for } (s, r, \phi) \in \Omega_\delta. \quad (\text{B4})$$

Proof. The calculation is as follows:

$$\begin{aligned} \int_{\Omega_\delta} \sigma w^2 \, d\mathbf{x} &= \int_{s=0}^{s_p} \int_{\phi=0}^{2\pi} \int_{r=1-\delta g(s, \phi)}^1 \sigma w^2 \, h_s h_r h_\phi \, dr d\phi ds \\ &\leq \int_{s=0}^{s_p} \int_{\phi=0}^{2\pi} \int_{r=1-\delta g(s, \phi)}^1 \sigma \left[\left(\frac{1-r}{1-\kappa \cos(\phi - \tau s)} + O(\delta^2) \right) \right. \\ &\quad \left. \times \int_{1-\delta g(s, \phi)}^1 \left(\frac{\partial w}{\partial r'} \right)^2 (1 - r'\kappa \cos(\phi - \tau s)) r' dr' \right] h_s h_r h_\phi \, dr d\phi ds. \end{aligned} \quad (\text{B5})$$

Note that Inequality 0 was used in the second line. For $(s, r, \phi) \in \Omega_\delta$, with an application of the triangle inequality we have

$$\begin{aligned} &|\sigma h_s h_r h_\phi - (1 - \kappa \cos(\phi - \tau s))\sigma(s, 1, \phi)| \\ &\leq |\sigma(s, r, \phi) - \sigma(s, 1, \phi)| \max_{(s, r, \phi) \in \Omega_\delta} (h_s h_r h_\phi) + |h_s h_r h_\phi - (1 - \kappa \cos(\phi - \tau s))\sigma(s, 1, \phi)|. \end{aligned} \quad (\text{B6})$$

Noting that

$$|\sigma(s, r, \phi) - \sigma(s, 1, \phi)| = O(\delta) \quad \text{and} \quad |h_s h_r h_\phi - (1 - \kappa \cos(\phi - \tau s))\sigma(s, 1, \phi)| = O(\delta),$$

when $(s, r, \phi) \in \Omega_\delta$, and

$$\max_{(s, r, \phi) \in \Omega_\delta} (h_s h_r h_\phi) = O(1) \quad \text{and} \quad \sigma(s, 1, \phi) = O(1),$$

leads to

$$|\sigma h_s h_r h_\phi - (1 - \kappa \cos(\phi - \tau s))\sigma(s, 1, \phi)| = O(\delta) \quad \text{for } (s, r, \phi) \in \Omega_\delta. \quad (\text{B7})$$

Using (B7) in (B5) and performing the integration in r leads to the desired result. \square

Appendix C. Some useful calculations

C.1. Calculation of $\nabla\mathbf{U}$

For the background flow given by (4.1), for $\mathbf{x} \in \Omega \setminus \Omega_\delta$, we have

$$\begin{aligned} \nabla\mathbf{U} = & \Lambda\kappa \cos(\phi - \tau s)\mathbf{e}_s\mathbf{e}_r - \Lambda\kappa \sin(\phi - \tau s)\mathbf{e}_s\mathbf{e}_\phi - \Lambda\kappa \cos(\phi - \tau s)\mathbf{e}_r\mathbf{e}_s \\ & + \Lambda\tau\mathbf{e}_r\mathbf{e}_\phi + \Lambda\kappa \sin(\phi - \tau s)\mathbf{e}_\phi\mathbf{e}_s - \Lambda\tau\mathbf{e}_\phi\mathbf{e}_r. \end{aligned} \quad (\text{C1})$$

It is clear that $\nabla\mathbf{U}_{\text{sym}} = \mathbf{0}$ in $\Omega \setminus \Omega_\delta$. For, $\mathbf{x} \in \Omega_\delta$, we have

$$\begin{aligned} \nabla\mathbf{U} = & -\frac{\Lambda(1-r)}{\delta g^2} \frac{\partial g}{\partial s} \mathbf{e}_s\mathbf{e}_s + \frac{\Lambda\kappa(1-r) \cos(\phi - \tau s)}{\delta g} \mathbf{e}_s\mathbf{e}_r \\ & - \left[\frac{\Lambda\tau r(1-r)}{\delta(1-r\kappa \cos(\phi - \tau s))g^2} \frac{\partial g}{\partial s} + \frac{\Lambda\kappa \sin(\phi - \tau s)(1-r)}{\delta g} \right] \mathbf{e}_s\mathbf{e}_\phi \\ & - \left[\frac{\Lambda(1-r\kappa \cos(\phi - \tau s))}{\delta g} + \frac{\Lambda\kappa \cos(\phi - \tau s)(1-r)}{\delta g} \right] \mathbf{e}_r\mathbf{e}_s \\ & + \left[\frac{\Lambda\tau(1-r)}{\delta g} - \frac{\Lambda\tau r}{\delta g} \right] \mathbf{e}_r\mathbf{e}_\phi - \frac{\Lambda\tau(1-r)}{\delta g} \mathbf{e}_\phi\mathbf{e}_r - \frac{\Lambda\tau(1-r)}{\delta g^2} \frac{\partial g}{\partial \phi} \mathbf{e}_\phi\mathbf{e}_\phi \\ & + \left[\frac{\Lambda\kappa \sin(\phi - \tau s)(1-r)}{\delta g} - \frac{\Lambda(1-r\kappa \cos(\phi - \tau s))(1-r)}{\delta r g^2} \frac{\partial g}{\partial \phi} \right] \mathbf{e}_\phi\mathbf{e}_s. \end{aligned} \quad (\text{C2})$$

Given that $1-r$ is $O(\delta)$ in the boundary layer, calculation of $|\nabla\mathbf{U}|^2$ up to leading order terms is

$$|\nabla\mathbf{U}|^2 = \frac{\Lambda^2(1-\kappa \cos(\phi - \tau s))^2}{\delta^2 g^2} + \frac{\Lambda^2 \tau^2}{\delta^2 g^2} + O(\delta^{-1}), \quad (\text{C3})$$

and

$$|\nabla\mathbf{U}|^2 h_s h_r h_\phi = \frac{\Lambda^2(1-\kappa \cos(\phi - \tau s))}{\delta^2 g^2} [(1-\kappa \cos(\phi - \tau s))^2 + \tau^2] + O(\delta^{-1}). \quad (\text{C4})$$

We use this result in (4.32) for the calculation of $\|\nabla\mathbf{U}\|^2$. With the use of (4.3), we see that the only two terms that are $O(\delta^{-1})$ in (C2) are the terms involving $\mathbf{e}_r\mathbf{e}_s$ and $\mathbf{e}_r\mathbf{e}_\phi$. However, these terms do not contribute to the calculation of $\mathbf{U} \cdot \nabla\mathbf{U}$, as they are multiplied with U_r (the r component of \mathbf{U}) which is zero. Therefore, $\mathbf{U} \cdot \nabla\mathbf{U}$ is $O(1)$ in Ω_δ . This result is useful in showing (4.26).

C.2. Reason behind choice 4.20

In the analysis done in the main text, if we had just assumed that p_1 , p_2 , and p_3 are constant functions but not necessarily equal, then a similar calculation would have led to

$$\begin{aligned} g(s, \phi) &= \sqrt{\frac{p_1 p_2 p_3}{p_3(1-\kappa \cos(\phi - \tau s))^2 + p_1 \tau^2}} \\ c_1(s, \phi) &= \sqrt{\frac{p_1}{p_2} + \frac{p_1^2 \tau^2}{p_2 p_3(1-\kappa \cos(\phi - \tau s))^2}}, \quad c_2(s, \phi) = \sqrt{\frac{p_3}{p_2} + \frac{p_3^2(1-\kappa \cos(\phi - \tau s))^2}{p_1 p_2 \tau^2}}. \end{aligned} \quad (\text{C5})$$

With this choice, we could have obtained the same bounds on the flow rate and the friction factor, namely

$$Q \geq \sqrt{\frac{32\pi^2}{27I(\kappa, \tau)}} + O(Re^{-1}) \quad \lambda \leq \lambda_b = \frac{27}{8}I(\kappa, \tau) + O(Re^{-1}). \quad (\text{C6})$$

However, this time

$$I(\kappa, \tau) = \frac{1}{2\pi} \int_0^{2\pi} (1 - \kappa \cos \alpha) \left((1 - \kappa \cos \alpha)^2 + \tau^2 \right) \sqrt{\frac{M^2(1 - \kappa \cos \alpha)^2}{p'_1} + \frac{M^2\tau^2}{p'_3}} d\alpha, \quad (\text{C7})$$

where

$$M = \max\{p'_1, 1, p'_3\}, \quad p'_1 = \frac{p_1}{p_2}, \quad p'_3 = \frac{p_3}{p_2}. \quad (\text{C8})$$

To optimize the bound, we need to minimize $I(\kappa, \tau)$ and that clearly happens when

$$p'_1 = p'_3 = 1 \quad \implies \quad p_1 = p_2 = p_3. \quad (\text{C9})$$

REFERENCES

- AVILA, K., MOXEY, D., DE LOZAR, A., AVILA, M., BARKLEY, D. & HOF, B. 2011 The onset of turbulence in pipe flow. *Science* **333**, 192–196.
- BERGER, S. A., TALBOT, L. & YAO, L. S. 1983 Flow in curved pipes. *Annu. Rev. Fluid Mech.* **15**, 461–512.
- BUSSE, F. H. 1969 On Howard's upper bound for heat transport by turbulent convection. *J. Fluid Mech.* **37** (3), 457–477.
- BUSSE, F. H. 1970 Bounds for turbulent shear flow. *J. Fluid Mech.* **41** (1), 219–240.
- CANTON, J., ÖRLÜ, R. & SCHLATTER, P. 2017 Characterisation of the steady, laminar incompressible flow in toroidal pipes covering the entire curvature range. *Intl J. Heat Fluid Flow* **66**, 95–107.
- CANTON, J., RINALDI, E., ÖRLÜ, R. & SCHLATTER, P. 2020 Critical point for bifurcation cascades and featureless turbulence. *Phys. Rev. Lett.* **124**, 014501.
- CANTON, J., SCHLATTER, P. & ÖRLÜ, R. 2016 Modal instability of the flow in a toroidal pipe. *J. Fluid Mech.* **792**, 894–909.
- CAULFIELD, C. P. 2005 Buoyancy flux bounds for surface-driven flow. *J. Fluid Mech.* **536**, 367–376.
- CAULFIELD, C. P. & KERSWELL, R. R. 2001 Maximal mixing rate in turbulent stably stratified couette flow. *Phys. Fluids* **13** (4), 894–900.
- CIONCOLINI, A. & SANTINI, L. 2006 An experimental investigation regarding the laminar to turbulent flow transition in helically coiled pipes. *Exp. Therm. Fluid Sci.* **30**, 367–380.
- CONSTANTIN, P. & DOERING, C. R. 1995 Variational bounds on energy dissipation in incompressible flows. II. Channel flow. *Phys. Rev. E* **51** (4), 3192–3198.
- DEAN, W. R. 1927 Note on the motion of fluid in a curved pipe. *Phil. Mag.* **4**, 208–223.
- DEAN, W. R. 1928 The stream-line motion of fluid in a curved pipe. *Phil. Mag.* **5**, 673–695.
- DENNIS, S. C. R. 1980 Calculation of the steady flow through a curved tube using a new finite-difference method. *J. Fluid Mech.* **99**, 449–467.
- DOERING, C. R. & CONSTANTIN, P. 1992 Energy dissipation in shear driven turbulence. *Phys. Rev. Lett.* **69** (11), 1648–1651.
- DOERING, C. R. & CONSTANTIN, P. 1994 Variational bounds on energy dissipation in incompressible flows: Shear flow. *Phys. Rev. E* **49** (5), 4087–4099.
- DOERING, C. R. & CONSTANTIN, P. 1996 Variational bounds on energy dissipation in incompressible flows. III. Convection. *Phys. Rev. E* **53** (6), 5957–5981.

- DOERING, C. R. & CONSTANTIN, P. 2001 On upper bounds for infinite Prandtl number convection with or without rotation. *J. Math. Phys.* **42** (2), 784–795.
- EUSTICE, J. 1910 Flow of water in curved pipes. *Proc. R. Soc. Lond. A* **84**, 107–118.
- EUSTICE, J. 1911 Experiments on streamline motion in curved pipes. *Proc. R. Soc. Lond. A* **85**, 119–131.
- FANTUZZI, G. 2018 Bounds for Rayleigh–Bénard convection between free-slip boundaries with an imposed heat flux. *J. Fluid Mech.* **837**, R5.
- FANTUZZI, G., NOBILI, C. & WYNN, A. 2020 New bounds on the vertical heat transport for Bénard–Marangoni convection at infinite Prandtl number. *J. Fluid Mech.* **885**, R4.
- FANTUZZI, G., PERSHIN, A. & WYNN, A. 2018 Bounds on heat transfer for Bénard–Marangoni convection at infinite Prandtl number. *J. Fluid Mech.* **837**, 562–596.
- FANTUZZI, G. & WYNN, A. 2015 Construction of an optimal background profile for the Kuramoto–Sivashinsky equation using semidefinite programming. *Phys. Lett. A* **379** (1–2), 23–32.
- FANTUZZI, G. & WYNN, A. 2016 Optimal bounds with semidefinite programming: an application to stress-driven shear flows. *Phys. Rev. E* **93** (4), 043308.
- GAMMACK, D. & HYDON, P. E. 2001 Flow in pipes with non-uniform curvature and torsion. *J. Fluid Mech.* **433**, 357–382.
- GERMANO, M. 1982 On the effect of torsion on a helical pipe flow. *J. Fluid Mech.* **125**, 1–8.
- GERMANO, M. 1989 The dean equations extended to a helical pipe flow. *J. Fluid Mech.* **203**, 289–305.
- GOLUSKIN, D. 2015 Internally heated convection beneath a poor conductor. *J. Fluid Mech.* **771**, 36–56.
- GOLUSKIN, D. & DOERING, C. R. 2016 Bounds for convection between rough boundaries. *J. Fluid Mech.* **804**, 370–386.
- HAGSTROM, G. & DOERING, C. R. 2010 Bounds on heat transport in Bénard–Marangoni convection. *Phys. Rev. E* **81** (4), 047301.
- HAGSTROM, G. I. & DOERING, C. R. 2014 Bounds on surface stress-driven shear flow. *J. Nonlinear Sci.* **24** (1), 185–199.
- HOPF, E. 1957 *Lecture series of the symposium on partial differential equations, Berkeley, 1955*. University of Kansas.
- HOWARD, L. N. 1963 Heat transport by turbulent convection. *J. Fluid Mech.* **17** (3), 405–432.
- HÜTTL, T. J. & FRIEDRICH, R. 2001 Direct numerical simulation of turbulent flows in curved and helically coiled pipes. *Comput. Fluids* **30**, 591–605.
- ITŌ, H. 1959 Friction factors for turbulent flow in curved pipes. *Trans. ASME J. Basic Engng* **81**, 123–134.
- KAO, H. C. 1987 Torsion effect on fully developed flow in a helical pipe. *J. Fluid Mech.* **184**, 335–356.
- KÜHNEN, J., BRAUNSHIER, P., SCHWEGEL, M., KUHLMANN, H. C. & HOF, B. 2015 Subcritical versus supercritical transition to turbulence in curved pipes. *J. Fluid Mech.* **770**, R3.
- LIU, S. & MASLIYAH, J. H. 1993 Axially invariant laminar flow in helical pipes with a finite pitch. *J. Fluid Mech.* **251**, 315–353.
- MARCHIORO, C. 1994 Remark on the energy dissipation in shear driven turbulence. *Physica D* **74** (3–4), 395–398.
- MCCONALOGUE, D. J. & SRIVASTAVA, R. S. 1968 Motion of a fluid in a curved tube. *Proc. R. Soc. Lond. A* **307**, 37–53.
- NAPHON, P. & WONGWISES, S. 2006 A review of flow and heat transfer characteristics in curved tubes. *Renewable and Sustainable Energy Rev.* **10** (5), 463–490.
- OTERO, J., WITTENBERG, R. W., WORTHING, R. A. & DOERING, C. R. 2002 Bounds on Rayleigh–Bénard convection with an imposed heat flux. *J. Fluid Mech.* **473**, 191–199.
- PLASTING, S. C. & IERLEY, G. R. 2005 Infinite-Prandtl-number convection. Part 1. Conservative bounds. *J. Fluid Mech.* **542**, 343–363.
- PLASTING, S. C. & KERSWELL, R. R. 2003 Improved upper bound on the energy dissipation rate in plane Couette flow: the full solution to Busse’s problem and the Constantin–Doering–Hopf problem with one-dimensional background field. *J. Fluid Mech.* **477**, 363–379.
- PLASTING, S. C. & KERSWELL, R. R. 2005 A friction factor bound for transitional pipe flow. *Phys. Fluids* **17** (1), 011706.

- RINALDI, E., CANTON, J. & SCHLATTER, P. 2019 The vanishing of strong turbulent fronts in bent pipes. *J. Fluid Mech.* **866**, 487–502.
- SREENIVASAN, K. R. & STRYKOWSKI, P. J. 1983 Stabilization effects in flow through helically coiled pipes. *Exp. Fluids* **1** (1), 31–36.
- TANG, W., CAULFIELD, C. P. & YOUNG, W. R. 2004 Bounds on dissipation in stress-driven flow. *J. Fluid Mech.* **510**, 333–352.
- TAYLOR, G. I. 1929 The criterion for turbulence in curved pipes. *Proc. R. Soc. Lond. A* **124**, 243–249.
- TENNEKES, H. & LUMLEY, J. L. 1972 *A first course in turbulence*. MIT press.
- TILGNER, A. 2017 Bounds on poloidal kinetic energy in plane layer convection. *Phys. Rev. Fluids* **2** (12), 123502.
- TILGNER, A. 2019 Time evolution equation for advective heat transport as a constraint for optimal bounds in Rayleigh–Bénard convection. *Phys. Rev. Fluids* **4** (1), 014601.
- TUTTLE, E. R. 1990 Laminar flow in twisted pipes. *J. Fluid Mech.* **219**, 545–570.
- VAN DYKE, M. 1978 Extended stokes series: laminar flow through a loosely coiled pipe. *J. Fluid Mech.* **86**, 129–145.
- VASHISTH, S., KUMAR, V. & NIGAM, K.D.P. 2008 A review on the potential applications of curved geometries in process industry. *Ind. Engng Chem. Res.* **47** (10), 3291–3337.
- VESTER, A. KALPAKLI, ÖRLÜ, R. & ALFREDSSON, P. H. 2016 Turbulent flows in curved pipes: recent advances in experiments and simulations. *Applied Mechanics Reviews* **68**.
- WANG, X. 1997 Time averaged energy dissipation rate for shear driven flows in \mathbb{R}^n . *Physica D* **99** (4), 555–563.
- WEBSTER, D. R. & HUMPHREY, J. A. C. 1993 Experimental observations of flow instability in a helical coil (Data bank contribution). *Trans. ASME J. Fluids Engng* **115**, 436–443.
- WEBSTER, D. R. & HUMPHREY, J. A. C. 1997 Traveling wave instability in helical coil flow. *Phys. Fluids* **9**, 407–418.
- WEN, B., CHINI, G., DIANATI, N. & DOERING, C. R. 2013 Computational approaches to aspect-ratio-dependent upper bounds and heat flux in porous medium convection. *Phys. Lett. A* **377** (41), 2931–2938.
- WEN, B., CHINI, G. P., KERSWELL, R. R. & DOERING, C. R. 2015 Time-stepping approach for solving upper-bound problems: Application to two-dimensional Rayleigh–Bénard convection. *Phys. Rev. E* **92** (4), 043012.
- WHITE, C. M. 1929 Streamline flow through curved pipes. *Proc. R. Soc. Lond. A* **123**, 645–663.
- WHITEHEAD, J. P. & DOERING, C. R. 2011 Ultimate state of two-dimensional Rayleigh–Bénard convection between free-slip fixed-temperature boundaries. *Phys. Rev. Lett.* **106** (24), 244501.
- WHITEHEAD, J. P. & WITTENBERG, R. W. 2014 A rigorous bound on the vertical transport of heat in Rayleigh–Bénard convection at infinite Prandtl number with mixed thermal boundary conditions. *J. Math. Phys.* **55** (9), 093104.
- WITTENBERG, R. W. 2010 Bounds on Rayleigh–Bénard convection with imperfectly conducting plates. *J. Fluid Mech.* **665**, 158–198.
- YAMAMOTO, K., AKITA, T., IKEUCHI, H. & KITA, Y. 1995 Experimental study of the flow in a helical circular tube. *Fluid Dynam. Res.* **16**, 237249.
- YAMAMOTO, K., YANASE, S. & YOSHIDA, T. 1994 Torsion effect on the flow in a helical pipe. *Fluid Dynam. Res.* **14**, 259–273.